Correlation-induced valley topology in buckled graphene superlattices

Manesco, Antonio L.R.; Lado, Jose L.

Important note
To cite this publication, please use the final published version (if applicable).
Please check the document version above.

Correlation-induced valley topology in buckled graphene superlattices

Correlation-induced valley topology in buckled graphene superlattices

Antonio L. R. Manesco[1, 2, *] and Jose L. Lado[3]

[1]*Computational Materials Science Group (CompuEEL),*
Escola de Engenharia de Lorena, Universidade de São Paulo (EEL-USP),
Materials Engineering Department (Demar), Lorena – SP, Brazil
[2]*Kavli Institute of Nanoscience, Delft University of Technology, Delft 2600 GA, The Netherlands*
[3]*Department of Applied Physics, Aalto University, Espoo, Finland*
(Dated: May 20, 2021)

Quasi-flat-bands emerging in buckled monolayer graphene superlattices have been recently shown to realize correlated states analogous to those observed in twisted graphene multilayers. Here, we demonstrate the emergence of valley topology driven by competing electronic correlations in buckled graphene superlattices. We show, both by means of atomistic models and a low-energy description, that the existence of long-range electronic correlations leads to a competition between antiferromagnetic and charge density wave instabilities, that can be controlled by means of screening engineering. Interestingly, we find that the emergent charge density wave has a topologically non-trivial electronic structure, leading to a coexistent quantum valley Hall insulating state. In a similar fashion, the antiferromagnetic phase realizes a spin-polarized quantum valley-Hall insulating state. Our results put forward buckled graphene superlattices as a new platform to realize interaction-induced topological matter.

I. INTRODUCTION

Mesoscopic systems provide a highly powerful platform to design quantum matter,[1–9] with the paradigmatic example of artificial topological superconductivity.[10–19] Moire two-dimensional materials have risen as a tunable platform to engineer states of matter,[2] ultimately allowing to explore a variety of controllable correlated states.[20–23] This emergence of tunable correlations stems from the quench of kinetic energy in emergent quasi-flat-bands, controllable by twist engineering.[24–26] A variety of twisted van der Waals materials have been demonstrated in this direction, including bilayers, trilayers and tetralayers.[27–32]

Beyond the wide family of twisted moire multilayer heterostructures[2], monolayer graphene has also been experimentally shown to realize moire-induced correlation physics in the single layer limit.[33] The field of straintronics, *i.e.*, the control of electronic properties of materials with strain,[34] has shown different methods to create two-dimensional periodically-strained superlattices with quasi-flat-bands, from substrate engineering[35] to inducing buckling transitions during fabrication.[33] From a low-energy perspective, inhomogeneous strain fields act as valley-dependent pseudo-magnetic fields, leading to the emergence of pseudo-Landau levels.[36–39]

There are several ways to create inhomogeneous strain fields in graphene with wrinkles, ripples, foldings, and bucklings.[40–42] In this work, we focus in the latter, motivated by a recent experiment.[33] We highlight that this buckling have large periodicity, in contrast to the atomic-scale buckling known to occur in pristine two-dimensional materials such as silicene, germanene, and stanene.[43–49] From a critical value of in-plane strain, the elastic energy is spontaneously reduced with out-of-plane distortions,[50–52] as depicted in Fig. 1a. The electronic structure reconstruction due to the strain field

leads to the formation of nearly flat bands.[33,53] Moreover, the bandwidth suppression enhances the interaction effects and leads to electrically-controllable correlated phases.[33,54]

Here we show that buckled graphene superlattices yield correlation-induced topological states, stemming from the combination of pseudo-Landau levels and non-local electronic interactions.[33,54] In particular, we show that the low energy states generated by the buckling (Fig. 1b) shows an emergent low-energy honeycomb structure. Also, similarly to free-standing graphene, the bandstructure (Fig. 1d) has Dirac cones at the corners of the mini-Brillouin zone.[54] We derive the low-energy model describing the bands closer to the Fermi energy (Sec. II), to explore the impact of electron-electron interactions, and show the existence of charge density wave and antiferromagnetic ground states (Sec. III). Interestingly, these phases driven by electronic interactions show finite valley Chern numbers, and associated topological surface states. We finally demonstrate the robustness of our model by comparing it with full atomistic selfconsistent calculations, showing analogous phenomenology as the one predicted by the effective model. Our results demonstrate that buckled graphene monolayer can sustain a rich family of correlated topological states, realizing analogous physics to twisted graphene multilayers in the single monolayer limit.

II. THE SYSTEM

We first review the effective model for the buckled graphene superlattice, depicted in Fig. 1a.[33,54] We take the graphene tight-binding Hamiltonian

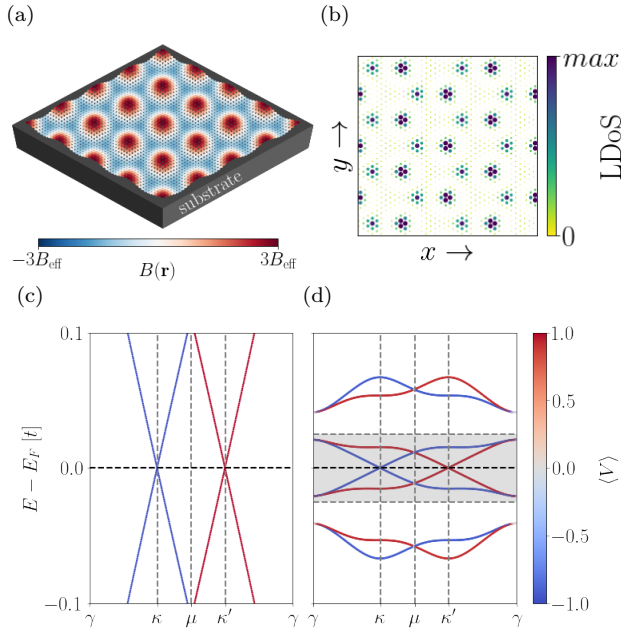$$\mathcal{H} = -t \sum_{\langle i,j \rangle} \sum_{s} \psi_{is}^{\dagger} \psi_{js}, \tag{1}$$

FIG. 1. (a) Scheme of the buckled graphene superlattice studied. The B-field is the same as in Eq. 6. (b) Local density of states from full-lattice calculations. It is possible to note the emerging honeycomb structure. Valley-projected band structures from a full-lattice simulation of a buckled graphene superlattice (c) in the absence of strain and (d) in the buckled state. The horizontal axis show the high-symmetry points in the mini-Brilouin zone defined by the superlattice. The dashed grey regions indicate the active bands for which we derive the effective model.
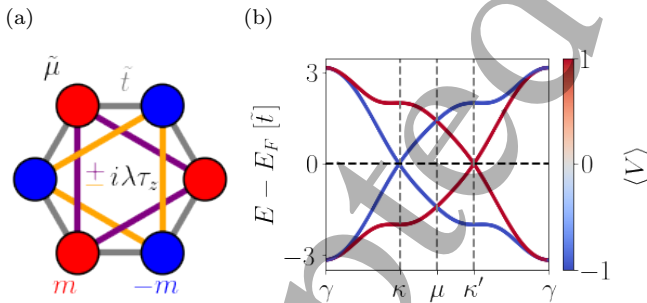

FIG. 2. (a) Schematic representation of the effective model in Eq. 8. (b) Valley-projected bandstructure of the effective model described by the Hamiltonian 8 with $m = M = t$.

where t is the nearest-neighbor hopping constant, i and j denote different sites, s denotes spin, $\langle i, j \rangle$ indicates the summation over nearest-neighbors, ψ_{is} is the annihilation and $\psi_{is}^{\dagger}$ is the creation operator in position i with spin s.

Under in-plane strain, the system undergoes a buckling transition, modifying the hopping energies with the

additional term[54]

$$\delta t_n = -\frac{\sqrt{3} e v_F L_M}{4\pi} \sin(\mathbf{b}_n \cdot \mathbf{r}), \qquad (2)$$

where L_M is the superlattice size, and v_F is the Fermi velocity of pristine graphene. The three vectors

$$\mathbf{b}_1 = \frac{2\pi}{L_M} \left(-\frac{1}{\sqrt{3}}, 1, 0 \right), \qquad (3)$$

$$\mathbf{b}_2 = \frac{2\pi}{L_M} \left(\frac{2}{\sqrt{3}}, 0, 0 \right), \qquad (4)$$

$$\mathbf{b}_3 = \frac{2\pi}{L_M} \left(-\frac{1}{\sqrt{3}}, -1, 0 \right) \qquad (5)$$

point along the same direction of each hopping vector.

In the $k \cdot p$ approximation, the Hamiltonian with hoppings given by Eq. 2 corresponds to a pseudo-magnetic field with the form[33]

$$B(\mathbf{r}) = B_{\text{eff}} \sum_{n=1}^{3} \cos(\mathbf{b}_n \cdot \mathbf{r}), \qquad (6)$$

where B_{eff} is estimated from the Landau level spacing from the experiment.[33] Under zero strain, the electronic structure is folded in the mini-Brillouin zone defined by the $\mathbf{b}_n$ vectors (see Fig. 1c). As the strain takes a finite value, avoided crossings are formed, creating mini-bands (see 1d) which we interpret as pseudo-Landau bands.[33,54] Hence, quasiparticles feel a bandwidth quench.

We perform the valley projection in full-lattice calculations (Figs. 1d and 6) computing the expectation value of the modified Haldane coupling, $\langle V \rangle = \langle \Psi | V | \Psi \rangle$, with[55–57]

$$V = \frac{i}{3\sqrt{3}} \sum_{\langle\langle i,j \rangle\rangle} \eta_{ij} (\sigma_z)_{ij} \psi_i^{\dagger} \psi_j, \qquad (7)$$

where $\eta_{ij} = \pm 1$ for clockwise/anticlockwise hopping, $\langle\langle i, j \rangle\rangle$ denotes a sum over second-neighbors, and σ_z acts om sublattice degrees of freedom.

From the local density of states plot in Fig. 1b, obtained with full-lattice tight-binding calculations,[54] it is possible to infer that the system has an emerging honeycomb superlattice. The Wannier sites are localized at the minima and maxima of $B(\mathbf{r})$ since the characteristic length $\sqrt{\hbar/eB(\mathbf{r})}$ is smaller near the extrema. The two extrema (minimum and maximum) correspond to the two sublattices of this effective honeycomb structure. To reduce the computational cost of our numerical calculations, we now focus on the low-energy model of these Wannier states. We focus on the active bands closer to the Fermi energy, highlighted in Fig. 2b. Namely, we derive an effective model for the bands within the $[-0.025t, 0.025t]$ energy window in Fig. 1d. This approach is analogous to low-energy models of twisted-bilayer graphene.

From both the space-dependent hopping constants (Eq. 2) and density of states (Fig. 1b), we conclude

that the system is invariant under C_3-rotations. Moreover, the bandstructure in Fig. 1d suggest that valley number is a conserved quantity. Finally, in the absence of electronic interactions, the system has time-reversal symmetry. With the current constraints, we find that the family of honeycomb Hamiltonians restricted to these symmetries is[58]

$$\mathcal{H} = -\mu \sum_i \sum_{s,\tau} c^\dagger_{is\tau} c_{is\tau} + m \sum_i \sum_{s,\tau} (\sigma_z)_{ii} c^\dagger_{is\tau} c_{is\tau} \quad (8)$$
$$- \tilde{t} \sum_{s,\tau} \sum_{\langle i,j \rangle} c^\dagger_{is\tau} c_{js\tau} + i\lambda \sum_{s,\tau} \sum_{\langle\langle i,j \rangle\rangle} (\tau_z)_{\kappa\kappa} \eta_{ij} c^\dagger_{is\tau} c_{js\tau}$$

where $c^\dagger_{is\tau}$ are creation and $c_{is\tau}$ annihilation operators operators at the site i, sublattice σ, valley τ, and spin s. The Pauli matrices σ_i and τ_i act on sublattice and valley degrees of freedom. The onsite energy and the nearest-neighbor hopping constants are denoted by $\tilde{\mu}$ and $\tilde{t}$ to distinguish to the atomistic model. There is also an onsite energy imbalance between both sublattices m, and a valley-dependent second-neighbors hopping λ. An scheme of this model is shown in Fig. 2a. Note that, since the Brillouin zone of this system corresponds to the mini-Brillouin zone from the atomistic model, there is an extra *mini-valley* degree of freedom corresponding to the two nonequivalent points κ and κ' in effective model Brillouin zone.

It is visible that the Hamiltonian of Eq. 8 is equivalent to the Kane-Mele (KM) model: it consists on the tight-binding model of a honeycomb structure with a sublattice imbalance and a second-neighbors hopping that depends on the valley isospin. The mapping between both models is made by identifying the valley isospin in the buckled superlattice to spin in KM model ($\text{spin}_{KM} \to \text{valley}_{\text{buckled}}$), as well as identifying the mini-valleys κ and κ' in the buckled system to the valleys K and K' in KM model ($\text{valley}_{KM} \to \text{mini-valley}_{\text{buckled}}$).[59,60] As shown in Fig. 2b, the energy dispersion is similar to the bandstructure of the full system [Fig. 1d] when $m = 3\sqrt{3}\lambda =: M$. Therefore, the non-interacting strained system (without symmetry breakings) is enforced to have $M = m = \tilde{t}$ due to its gapless nature. Note that arbitrarily small variations of m/M open a gap in the effective model. If $\delta(m/M) > 0$, the system becomes a trivial insulator. On the other hand, $\delta(m/M) < 0$ opens a topological gap and the system becomes a quantum valley Hall insulator, in analogy to the spin Hall insulator phase in the KM model.

Since the topographic shape of the buckling has the same functional form of $B(\mathbf{r})$, out-of-plane displacement fields lead to a modulation of onsite energies as:[54]

$$\mu(\mathbf{r}) = \mu_0 \sum_{n=1}^3 \cos(\mathbf{b}_n \cdot \mathbf{r}). \quad (9)$$

where $\mu_0 = D\,\delta h/4.5$ is proportional to the displacement field D and the buckling amplitude $\delta h = 0.4nm$ (the factor 4.5 comes from the amplitude of the summation
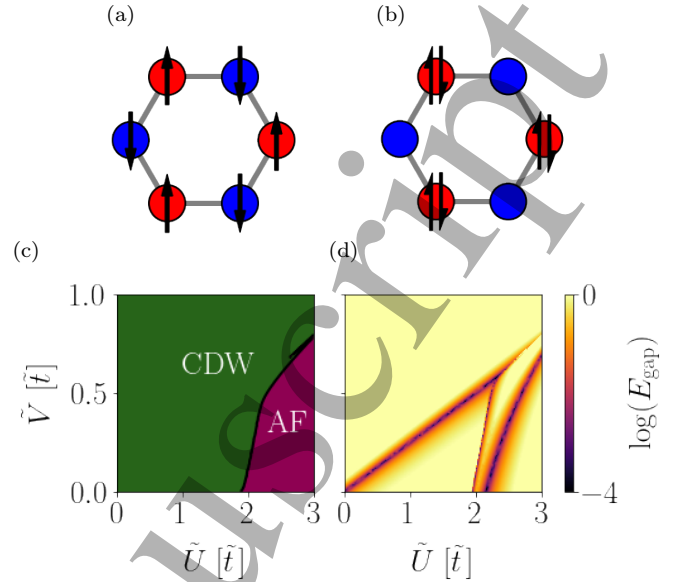
FIG. 3. Illustration of (a) antiferromagnetic and (b) charge density wave groundstates. (c) Phase diagram as a function of the coupling constants $\tilde{U}$ and $\tilde{V}$. The groundstate is a charge density wave (CDW) unless $\tilde{U}$ is sufficiently high. For $\tilde{U}$ higher than a critical value, an antiferromagnetic (AF) order develops. (d) System gap as a function of the electron-electron couplings. It is visible that the gap closes outside the region in which the broken symmetry changes.

in Eq. 9). Thus, near the maxima of $B(\mathbf{r})$, $\mu(\mathbf{r}) \approx 3\mu_0$, and $\mu(\mathbf{r}) \approx 3\mu_0/2$ near the minima of $B(\mathbf{r})$. From the effective model perspective, the onsite energy modulation is:

$$\mathcal{H}_{\text{elec}} = 3\mu_{\text{elec}} \sum_{i \in A} \sum_{s,\tau} c^\dagger_{is\tau} c_{is\tau} - \frac{3\mu_{\text{elec}}}{2} \sum_{i \in B} \sum_{s,\tau} c^\dagger_{is\tau} c_{is\tau},$$
$$(10)$$

where $\mu_{\text{elec}} \propto \mu_0$. The sum over i is performed on different sublattices in Eq. 10, since the corresponding Wannier sites are located at the maxima and minima of $\mu(\mathbf{r})$. This extra term modifies the Hamiltonian as $m \to m + 3\mu_{\text{elec}}/2$, and $\tilde{\mu} \to \tilde{\mu} - 3\mu_{\text{elec}}/2$. Therefore, out-of-plane displacement fields might be used as a knob to control the ratio m/M, ultimately working as an electric control of the system's topology, as shown in Fig. 4.

III. INTERACTION-DRIVEN QUANTUM VALLEY HALL EFFECT

The reduced bandwidth reduction due to the pseudo-magnetic field has been shown to lead to a correlated phase.[33,54] Yet, due to the degeneracy of the low energy states, different groundstates may be realized in the system, depending on the range and strength of

FIG. 4. Valley Chern number dependence on (a) sublattice imbalance m and antiferromagnetic mass m_{AF} for the effective model, taking constant λ. Panel (b) shows the valley Chern number obtained after including interactions in the interactiong model, as a function of the Hubbard constant $\tilde{U}$ and nearest-neighbors interactions $\tilde{V}$. Solid lines indicate a topological phase transition and dashed lines indicate $m = M$, which for m_{AF} corresponds to the non-interacting strained system.

interactions.[61–63] The computational cost of full-lattice calculations makes an extensive investigation of possible groundstates impractical. Hence, the reduced computational cost with an effective model allows us to explore the phase diagram as a function of electronic interactions.

To investigate the phase diagram of buckled graphene, we now include electronic interactions in the low energy model

$$\mathcal{H}_{int} = \tilde{U} \sum_{\substack{\alpha,\beta \\ \alpha \neq \beta}} \sum_i n_{i\alpha} n_{i\beta} + \tilde{V} \sum_{\langle i,j \rangle} \sum_{\alpha,\beta} n_{i\alpha} n_{j\beta} \quad (11)$$

where $\tilde{U}$ is the onsite Hubbard interaction, $\tilde{V}$ is the nearest-neighbor interaction, $n_{i\alpha} := c_{i\alpha}^\dagger c_{i\alpha}$ is the number operator at the Wannier site i. The subindices α and β are a short-hand notation to include both valley and spin degrees of freedom.

We solve this Hamiltonian by means of a mean-field approximation. Namely, we make

$$\mathcal{H}_{int} \approx \mathcal{H}_{MF} = \sum_{i,j,\alpha,\beta} \chi_{ij\alpha\beta} c_{i\alpha}^\dagger c_{j\beta}, \quad (12)$$

and find $\chi_{ij\alpha\beta}$ self-consistently. First, it is important to note that the interaction strengths $\tilde{U}$ and $\tilde{V}$ depend on the screening created by the substrate of the buckled structure,[64] and as such can be controlled by screening engineering.[64–67] In the following, we will explore the potential symmetry broken states as a function of the two interaction strengths, keeping in mind that such values would be controlled by substrate engineering. As we change the ratio of the local and non-local interaction, we see that there are two different groundstates, shown in the phase diagram of Fig. c. A charge density wave,

FIG. 5. Sublattice-projected bandstructure for selected $\tilde{U}$ and $\tilde{V}$ showing all four distinct phases: (a) charge density wave, (b) antiferromagnet, (c) quantum valley Hall insulator, and (d) spin-polarized quantum valley Hall insulator.

illustrated in Fig. b, develops and persists until the Hubbard constant reaches a critical value at which an antiferromagnetic ordering, depicted in Fig. a, occurs. For $\tilde{V} = 0$, this critical value is $\tilde{U}_c \sim 2t$, as expected for honeycomb systems.[68]

From a mean-field perspective, the charge density wave groundstate leads to a change in the sublattice imbalance. In other words, it leads to a transformation $m \to m + m_{CDW}$. The effects of an antiferromagnetic lead to the additional term in the Hamiltonian 8:

$$H_{AF} = m_{AF} \kappa_0 \otimes \tau_0 \otimes \sigma_z \otimes s_z, \quad (13)$$

where s_z acts on the spin space, and m_{AF} is the mean-field antiferromagnetic mass. Note that one can interpret the antiferromagnetic term as a spin-dependent sublattice imbalance.

As discussed in Sec. II, small variations on the ratio m/M lead to a gap opening. That makes one wonder if there are topological phase transitions as we change the electron-electron coupling constants. Hence, we compute, for different values of m and m_{AF}, the valley Chern number[69,70]

$$C_V = C_K - C_{K'}$$
$$= \int_{-\infty}^0 d\omega \int_{BZ} \frac{d^2\mathbf{k}}{(2\pi)^2} \frac{\epsilon_{\alpha\beta}}{2} G_V (\partial_{k_\alpha} G_V^{-1})(\partial_{k_\beta} G_V). \quad (14)$$

Here, $\epsilon_{\alpha\beta}$ denotes the Levi-Civita tensor,

$$G_V = [\omega - H(\mathbf{k}) + i0^+]^{-1} \mathcal{P}_V \quad (15)$$

the Green's function associated with the Bloch Hamiltonian $H(\mathbf{k})$, and $\mathcal{P}_V = \tau_z$ is the valley operator.
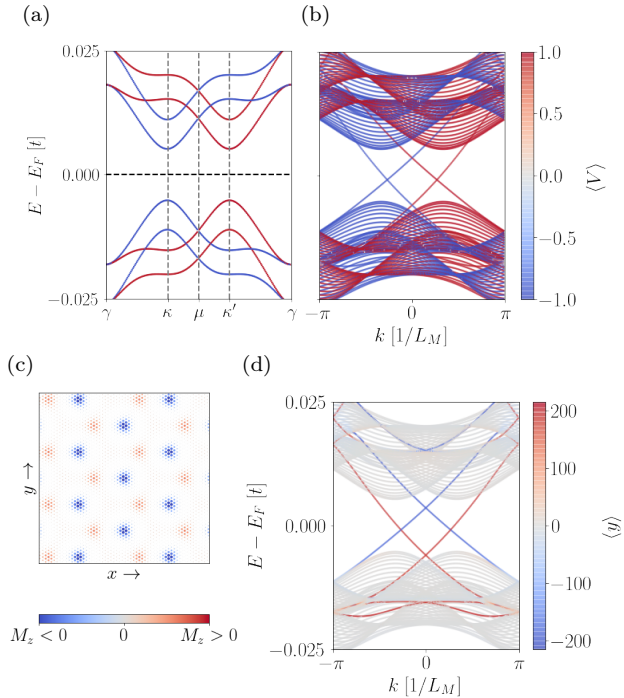
FIG. 6. Results of full-lattice calculations with modulated hoppings in Eq. 2 solved self-consistently with an additional Hubbard constant $U = 0.3t$. Valley Chern number in a (a) infinite system and (b) in a nanoribbon. (c) Magnetization along the z-direction. A periodically modulated ferrimagnetic order is formed. From a superlattice perspective, it cooresponds to a antiferromagnetic honeycomb structure. (d) y-position projection of a nanoribbon bandstructure. We see that each edge has two counter-propagating edge states with opposite valley-polarization.

We see in Fig. 3a that there are two topologically non-trivial phases: one of them is a QVHI for both spin channels (valley Chern number 4), the other is the one that we predict to exist in a single spin channel (valley Chern number 2). The formation of both phases is rather intuitive to understand. While the QVHI takes place when $\delta(m/M) < 0$, the sQVHI phase exist for both positive and negative values of m_{AF}. The reason is that while one spin channel suffers a shift $m \to m + m_{AF}$, the other is shifted as $m \to m - m_{AF}$. Thus, one spin channel becomes topological and the other becomes a trivial insulator. This is visible in Fig. 5: in the QVHI phase [Fig. 5 (c)], all four bands show a band inversion; and in the sQVHI phase [Fig. 5 (d)], only two out of the four bands show a band inversion. The band inversion occurs in the spin channels for which the sublattice imbalance decreases.

Now we note that, even though there are only two regions in the order parameter map of Fig. 3c, there are several gap closings in Fig. 3d. Reviewing the phase diagram by also checking the valley Chern number, it is visible that varying $\tilde{U}$ and $\tilde{V}$ yields four distinct phases:

trivial charge density wave and antiferromagnet, as well as topological charge density wave (QVHI) and topological antiferromagnet (sQVHI). We also show selected sublattice-projected band diagrams in Figs. 5 a-d. While the charge density wave (Fig. 5a) and antiferromagnetic (Fig. 6b) bulk bands have well-defined sublattice numbers, the QVHI (Fig. 5c) and the sQVHI (Fig. 5d) show a band inversion.

To compare with the effective model calculations, we perform self-consistent Hubbard mean-field calculations in a superlattice following our previous work.[54] To reduce the computational cost, we rescaled the system as $a \to \beta a$ and $t \to t/\beta$ so the Fermi velocity keeps constant.[71] We choose, as an example, the Hubbard constant to be $U = 0.3t$, resulting in a correlation gap in the bandstructure (see Fig. 6a). The gap is a result of a magnetic phase in the form of a superlattice-modulated ferrimagnetic order (see Fig. 6c). Integrating the magnetization in the vincinity to a minimum of $B(\mathbf{r})$ the magnetization is finite and positive, while it is negative in the neighborhood of pseudo-magnetic field maxima. In this situation, the system has a valley Chern number 2, in accordance with our effective model calculations with an antiferromagnetic ordering. We found that this system is in the sQVHI phase, with valley Chern number 2, compatible with the magnetically ordered groundstate observed.[54] The existence of topological edge states is visible in the bandstructure of a nanoribbon, shown in Fig. 6b and 6b. As expected, we observe two counter-propagating (helical-like) edge states with opposite valley numbers at both boundaries, similarly to the Kane-Mele model.[59,60] Finally, we note that the local charge accumulation with the periodic potential might also change the values of $\tilde{U}$ and $\tilde{V}$. Furthermore, the increase of out-of-plane fields closes the antiferromagnetic gap.[54] Thus, electrostatic control is not only a knob to control topology, but also electronic correlations.

IV. CONCLUSIONS

To summarize, we have shown that buckled graphene superlattices show spontaneous symmetry breaking driven by electronic interactions, leading to a topological gap opening. First, by combining atomistic low energy models with a symmetry analysis, we derived an effective model for the lowest bands of buckled graphene superlattices. We then included electronic interactions in a non-local form in the low-energy model, showing the emergence of competing ground states. Namely, an antiferromagnetic and a charge density wave. Remarkably, the spontaneous breaking of symmetries was shown to lead to a topological gap opening for a wide range of the non-local interactions. The charge density wave phase hosts a quantum valley Hall insulator, while the antiferromagnetic phase has a spin-polarized quantum valley Hall insulator region in the parameter space. Our results put forward buckled graphene superlattices as a platform

to study interaction-induced valley topology, and highlight that single layer moire systems can potentially host analogous correlated states to those of complex twisted graphene multilayers.

Data availability The data shown in the figures, as well as the code generating all of the data is available on Zenodo.[72]

* am@antoniomanesco.org

[1] Y. Zhang, N. F. Q. Yuan, and L. Fu, Physical Review B **102**, 201115 (2020).

[2] E. Y. Andrei, D. K. Efetov, P. Jarillo-Herrero, A. H. MacDonald, K. F. Mak, T. Senthil, E. Tutuc, A. Yazdani, and A. F. Young, Nature Reviews Materials **6**, 201 (2021).

[3] P.-Y. Chen, X.-Q. Zhang, Y.-Y. Lai, E.-C. Lin, C.-A. Chen, S.-Y. Guan, J.-J. Chen, Z.-H. Yang, Y.-W. Tseng, S. Gwo, C.-S. Chang, L.-J. Chen, and Y.-H. Lee, Advanced Materials **31**, 1901077 (2019).

[4] J. L. Lado and P. Liljeroth, arXiv:2102.11779 [cond-mat] (2021), arXiv:2102.11779 [cond-mat].

[5] Z.-D. Li, Q.-Y. Li, L. Li, and W. M. Liu, Phys. Rev. E **76**, 026605 (2007).

[6] Z. F. Jiang, R. D. Li, S.-C. Zhang, and W. M. Liu, Phys. Rev. B **72**, 045201 (2005).

[7] X.-L. Zhang, L.-F. Liu, and W.-M. Liu, Scientific Reports **3**, 2908 (2013).

[8] Y.-H. Chen, H.-S. Tao, D.-X. Yao, and W.-M. Liu, Phys. Rev. Lett. **108**, 246402 (2012).

[9] F. Wu, T. Lovorn, E. Tutuc, and A. H. MacDonald, Physical Review Letters **121**, 026402 (2018).

[10] A. Y. Kitaev, Annals of Physics **303**, 2 (2003).

[11] R. M. Lutchyn, J. D. Sau, and S. D. Sarma, Physical Review Letters **105**, 077001 (2010).

[12] K. T. Law, P. A. Lee, and T. K. Ng, Physical Review Letters **103**, 237001 (2009).

[13] H. Zhang, M. W. A. de Moor, J. D. S. Bommer, D. Xu, G. Wang, N. van Loo, C.-X. Liu, S. Gazibegovic, J. A. Logan, D. Car, R. L. M. O. het Veld, P. J. van Veldhoven, S. Koelling, M. A. Verheijen, M. Pendharkar, D. J. Pennachio, B. Shojaei, J. S. Lee, C. J. Palmstrøm, E. P. A. M. Bakkers, S. D. Sarma, and L. P. Kouwenhoven, arXiv:2101.11456 [cond-mat] (2021), arXiv:2101.11456 [cond-mat].

[14] H. Zhang, D. E. Liu, M. Wimmer, and L. P. Kouwenhoven, Nature Communications **10**, 5128 (2019).

[15] V. Mourik, K. Zuo, S. M. Frolov, S. R. Plissard, E. P. a. M. Bakkers, and L. P. Kouwenhoven, Science **336**, 1003 (2012).

[16] S. Kezilebieke, M. N. Huda, V. Vaňo, M. Aapro, S. C. Ganguli, O. J. Silveira, S. Głodzik, A. S. Foster, T. Ojanen, and P. Liljeroth, Nature **588**, 424 (2020).

[17] P. San-Jose, J. L. Lado, R. Aguado, F. Guinea, and J. Fernández-Rossier, Physical Review X **5**, 041042 (2015).

[18] Y. Oreg, G. Refael, and F. von Oppen, Physical Review Letters **105**, 177002 (2010).

[19] L. Fu and C. L. Kane, Physical Review Letters **100**, 096407 (2008).

[20] Z. Song, Z. Wang, W. Shi, G. Li, C. Fang, and B. A. Bernevig, Physical Review Letters **123**, 036401 (2019).

[21] F. Xie, Z. Song, B. Lian, and B. A. Bernevig, Physical Review Letters **124**, 167002 (2020).

[22] Y. Da Liao, J. Kang, C. N. Breiø, X. Y. Xu, H.-Q. Wu, B. M. Andersen, R. M. Fernandes, and Z. Y. Meng, Physical Review X **11**, 011014 (2021).

[23] Y. Choi, H. Kim, Y. Peng, A. Thomson, C. Lewandowski, R. Polski, Y. Zhang, H. S. Arora, K. Watanabe, T. Taniguchi, J. Alicea, and S. Nadj-Perge, Nature **589**, 536 (2021).

[24] V. J. Kauppila, F. Aikebaier, and T. T. Heikkilä, Physical Review B **93**, 214505 (2016).

[25] N. B. Kopnin, T. T. Heikkilä, and G. E. Volovik, Physical Review B **83**, 220503 (2011).

[26] E. Tang and L. Fu, Nature Physics **10**, 964 (2014).

[27] Y. S. Gani, H. Steinberg, and E. Rossi, Physical Review B **99**, 235404 (2019).

[28] Y. Cao, V. Fatemi, S. Demir, S. Fang, S. L. Tomarken, J. Y. Luo, J. D. Sanchez-Yamagishi, K. Watanabe, T. Taniguchi, E. Kaxiras, R. C. Ashoori, and P. Jarillo-Herrero, Nature **556**, 80 (2018).

[29] C. Shen, Y. Chu, Q. Wu, N. Li, S. Wang, Y. Zhao, J. Tang, J. Liu, J. Tian, K. Watanabe, T. Taniguchi, R. Yang, Z. Y. Meng, D. Shi, O. V. Yazyev, and G. Zhang, Nature Physics **16**, 520 (2020).

[30] X. Liu, Z. Hao, E. Khalaf, J. Y. Lee, Y. Ronen, H. Yoo, D. H. Najafabadi, K. Watanabe, T. Taniguchi, A. Vishwanath, and P. Kim, Nature **583**, 221 (2020).

[31] J. M. Park, Y. Cao, K. Watanabe, T. Taniguchi, and P. Jarillo-Herrero, Nature **590**, 249 (2021).

[32] Y. Cao, J. M. Park, K. Watanabe, T. Taniguchi, and P. Jarillo-Herrero, arXiv e-prints , arXiv:2103.12083 (2021), arXiv:2103.12083 [cond-mat.mes-hall].

[33] J. Mao, S. P. Milovanović, M. Anđelković, X. Lai, Y. Cao, K. Watanabe, T. Taniguchi, L. Covaci, F. M. Peeters, A. K. Geim, Y. Jiang, and E. Y. Andrei, Nature **584**, 215 (2020).

[34] A. A. Bukharaev, A. K. Zvezdin, A. P. Pyatakov, and Y. K. Fetisov, Physics-Uspekhi **61**, 1175 (2018).

[35] Y. Jiang, J. Mao, J. Duan, X. Lai, K. Watanabe, T. Taniguchi, and E. Y. Andrei, Nano Letters **17**, 2839 (2017).

[36] M. A. H. Vozmediano, M. I. Katsnelson, and F. Guinea, Physics Reports **496**, 109 (2010), arXiv:1003.5179.

[37] T. Low and F. Guinea, Nano Letters **10**, 3551 (2010).

[38] M. Ramezani Masir, D. Moldovan, and F. Peeters, Solid State Communications **175-176**, 76 (2013).

[39] T. J. Peltonen and T. T. Heikkilä, Journal of Physics: Condensed Matter **32**, 365603 (2020).

[40] S. Deng and V. Berry, Materials Today **19**, 197 (2016).

[41] A. P. Sgouros, G. Kalosakas, K. Papagelis, and C. Galiotis, Scientific Reports **8**, 9593 (2018).

[42] C. Zhang, C. Lu, L. Pei, J. Li, and R. Wang, Nano Materials Science **3**, 95 (2021).

[43] M. A. Kharadi, G. F. A. Malik, F. A. Khanday, K. A. Shah, S. Mittal, and B. K. Kaushik, ECS Journal of Solid State Science and Technology **9**, 115031 (2020).

[44] G. G. Guzmán-Verri and L. C. Lew Yan Voon, Phys. Rev. B **76**, 075131 (2007).

[45] J. Zhao, H. Liu, Z. Yu, R. Quhe, S. Zhou, Y. Wang, C. C. Liu, H. Zhong, N. Han, J. Lu, Y. Yao, and K. Wu, Progress in Materials Science **83**, 24 (2016).

[46] A. Acun, L. Zhang, P. Bampoulis, M. Farmanbar, A. van Houselt, A. N. Rudenko, M. Lingenfelder, G. Brocks, B. Poelsema, M. I. Katsnelson, and H. J. W. Zandvliet, Journal of Physics: Condensed Matter **27**, 443002 (2015).

[47] C. Grazianetti, E. Cinquanta, and A. Molle, 2D Materials **3**, 012001 (2016).

[48] A. Molle, J. Goldberger, M. Houssa, Y. Xu, S.-C. Zhang, and D. Akinwande, Nature Materials **16**, 163 (2017).

[49] J.-K. Lyu, S.-F. Zhang, C.-W. Zhang, and P.-J. Wang, Annalen der Physik **531**, 1900017 (2019), https://onlinelibrary.wiley.com/doi/pdf/10.1002/andp.201900017.

[50] W. Bao, F. Miao, Z. Chen, H. Zhang, W. Jang, C. Dames, and C. N. Lau, Nature Nanotechnology **4**, 562 (2009).

[51] S. Cai, D. Breid, A. J. Crosby, Z. Suo, and J. W. Hutchinson, Journal of the Mechanics and Physics of Solids **59**, 1094 (2011).

[52] E. Cerda and L. Mahadevan, Physical Review Letters **90**, 074302 (2003).

[53] S. P. Milovanović, M. Anđelković, L. Covaci, and F. M. Peeters, Phys. Rev. B **102**, 245427 (2020).

[54] A. L. R. Manesco, J. L. Lado, E. V. S. Ribeiro, G. Weber, and D. R. Jr, 2D Materials **8**, 015011 (2020).

[55] E. Colomés and M. Franz, Physical Review Letters **120**, 086603 (2018).

[56] A. Ramires and J. L. Lado, Phys. Rev. Lett. **121**, 146801 (2018).

[57] A. Lopez-Bezanilla and J. L. Lado, Phys. Rev. Research **2**, 033357 (2020).

[58] D. Varjas, T. Ö. Rosdahl, and A. R. Akhmerov, New Journal of Physics **20**, 093026 (2018).

[59] C. L. Kane and E. J. Mele, Physical Review Letters **95**, 226801 (2005).

[60] C. L. Kane and E. J. Mele, Physical Review Letters **95**, 146802 (2005).

[61] M. Kharitonov, Physical Review B **85**, 155439 (2012).

[62] M. O. Goerbig, Reviews of Modern Physics **83**, 1193 (2011).

[63] A. F. Young, J. D. Sanchez-Yamagishi, B. Hunt, S. H. Choi, K. Watanabe, T. Taniguchi, R. C. Ashoori, and P. Jarillo-Herrero, Nature **505**, 528 (2014).

[64] P. Stepanov, I. Das, X. Lu, A. Fahimniya, K. Watanabe, T. Taniguchi, F. H. L. Koppens, J. Lischner, L. Levitov, and D. K. Efetov, Nature **583**, 375 (2020).

[65] J. M. Pizarro, M. Rösner, R. Thomale, R. Valentí, and T. O. Wehling, Phys. Rev. B **100**, 161102 (2019).

[66] M. Rösner and J. L. Lado, Phys. Rev. Research **3**, 013265 (2021).

[67] C. Steinke, T. O. Wehling, and M. Rösner, Phys. Rev. B **102**, 115111 (2020).

[68] M. Schüler, M. Rösner, T. O. Wehling, A. I. Lichtenstein, and M. I. Katsnelson, Physical Review Letters **111**, 036601 (2013).

[69] K.-T. Chen and P. A. Lee, Physical Review B **84**, 205137 (2011).

[70] T. M. R. Wolf, J. L. Lado, G. Blatter, and O. Zilberberg, Physical Review Letters **123**, 096802 (2019).

[71] M.-H. Liu, P. Rickhaus, P. Makk, E. Tóvári, R. Maurand, F. Tkatschenko, M. Weiss, C. Schönenberger, and K. Richter, Physical Review Letters **114**, 036601 (2015).

[72] A. L. R. Manesco and J. L. Lado, "Correlation-induced valley topology in buckled graphene superlattices," (2021).